

# Omni-Directional Mobility Using Active Split Offset Castors

Haoyong Yu

Matthew Spenko

Steven Dubowsky

Department of Mechanical Engineering,  
Massachusetts Institute of Technology,  
Cambridge, MA 02139  
e-mail: dubowsky@mit.edu

*An omni-directional mobility platform design concept using two active split offset castors (ASOC) and one or more conventional castors is presented. An ASOC module consists of two coaxial conventional wheels driven independently and connected to the platform via an offset link. The kinematics and implementation of the omni-directional platform is described and analyzed. Particular attention is paid to the system performance on uneven floors. The fundamental mechanics of the ASOC wheel scrubbing, which is critical to system wear and energy use, is analyzed and compared to conventional active castor designs. The effectiveness of the design is shown experimentally using an intelligent mobility aid for the elderly. [DOI: 10.1115/1.1767181]*

## 1 Introduction

Computer controlled omni-directional mobile platforms are needed for robotic systems that operate in environments congested with obstacles such as those found in offices, factory workshops and warehouses, eldercare facilities, and hospitals [1]. The mobility of common wheeled vehicles using conventional or skid steering is limited in such environments due to the non-holonomic constraints of their wheels. While they can generally reach any position and orientation in the environment, it may require complex maneuvers. Vehicles with omni-directional mobility, the ability to move instantaneously in any direction from any configuration, would be desirable for such applications.

A variety of omni-directional vehicle designs have been developed. Of these, there are two types: those using special wheels and those using conventional wheels. Most special wheel designs are based on a concept that achieves traction in one direction and allows passive motion in another [2,3]. A well known class of special wheel designs is one that has passive rollers mounted on the periphery of a normal wheel such that the axes of the rollers are perpendicular or at an angle to that of the wheel, such as the Mecanum wheel design [4]. Other special wheel designs include the orthogonal wheel [5] and the ball wheel mechanism [1]. Such special wheel designs can have good omni-directional mobility, but they are generally complex. Vehicles using them commonly have limited load capacity since they use slender rollers to support the loads. Also, the height of traversable obstacles is limited by the small diameter of the rollers. The passive rollers also can generate unwanted vibrations and trap dirt in the wheels. Hence, specialty wheel designs can be impractical in applications where the floors have dirt and debris, are covered in thick carpeting, or the vehicle must carry heavy loads.

Platform designs have been proposed to achieve near omni-directional mobility using conventional wheels. Such designs are inherently simpler than special wheel designs. They can have high load capacity and high tolerance to floor irregularities such as bumps, cracks, dirt, and debris. The most common approach is to use actively steered wheels [6]. Vehicles based on this design have at least two active wheels, each of which has both driving and steering actuators that allow the wheels to move in any direction from any configuration, but not instantaneously. However, these vehicles are not truly omni-directional because they need to stop and re-orient their wheels when following a trajectory without C1 continuity. A truly omni-directional vehicle can be formed using

the active castor design where the wheel is offset from the steering actuator [1]. With two or more such wheels omni-directional mobility can be achieved for a vehicle [7,8].

A major drawback of the above conventional wheel designs is the high wheel scrubbing when the driving wheel is twisted about its vertical axis [5]. Wheel scrubbing can reduce the system's positioning accuracy and increase its power consumption and tire wear, especially for heavy vehicles and vehicles operating on rough surfaces such as carpeting. Dual wheel designs, commonly found in aircraft landing gear, are known to substantially reduce wheel scrubbing compared to single wheel designs; however, the fundamental mechanics of scrubbing in either type of castors has not been investigated until now.

In this paper, a truly omni-directional mobility platform using a pair of Active Split Offset Castors (ASOC) is presented. This design has been implemented on an intelligent walker for the elderly, called the SmartWalker [9]. See Fig. 1. This paper addresses the ASOC's kinematics, implementation issues, and behavior operating on an uneven floor. A fundamental analysis of the scrubbing properties of the ASOC is also presented along with a comparison with a single wheel castor design. Finally, the effectiveness of the ASOC design is demonstrated by the experimental results of the SmartWalker.

## 2 Concept and Kinematics of an Active Split Offset Castor

An active split offset castor (ASOC) module consists of two independently driven coaxial wheels, which are separated at a distance  $D$  and connected via an offset link  $S$  to the platform at the joint, as shown in Fig. 2.

In the coordinate systems defined in Fig. 2,  $XOY$  is an inertial coordinate frame and  $X_wCY_w$  is a moving coordinate frame attached to the wheel module at the offset link joint (point  $C$ ). The wheel velocities are  $V_1$  and  $V_2$ , and the joint velocities with respect to ground are  $V_f$  and  $V_s$ . The two vectors  $\mathbf{u}$  and  $\dot{\mathbf{q}}_w$  are defined as:

$$\mathbf{u} = [V_1 \quad V_2]^T$$

$$\dot{\mathbf{q}}_w = [V_f \quad V_s]^T \quad (1)$$

The relation between  $\dot{\mathbf{q}}_w$  and  $\mathbf{u}$  can be written as:

$$\dot{\mathbf{q}}_w = \mathbf{J}_w \mathbf{u} = \begin{bmatrix} 1/2 & 1/2 \\ S/D & -S/D \end{bmatrix} \mathbf{u} \quad (2)$$

where  $\mathbf{J}_w$  is the Jacobian matrix of the ASOC module in the moving coordinate frame  $X_wCY_w$ . The velocity of point  $C$  expressed in the inertial frame is defined as  $\dot{\mathbf{q}}$  and is given by:

Contributed by the Mechanisms and Robotics Committee for publication in the JOURNAL OF MECHANICAL DESIGN. Manuscript received July 2003; rev. January 2004. Associate Editor: M. Raghavan.

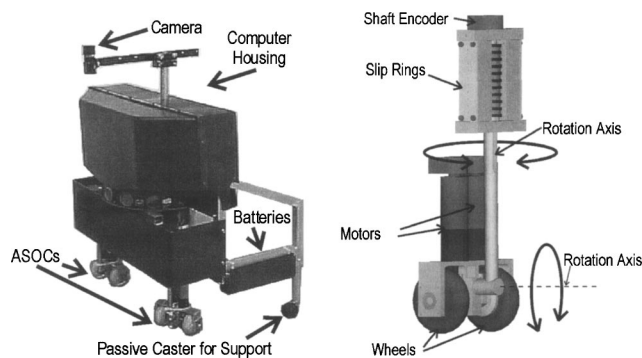


Fig. 1 The SmartWalker and its active offset split castor

$$\dot{\mathbf{q}} = [\dot{v}_x \quad \dot{v}_y]^T = \mathbf{R} \dot{\mathbf{q}}_w = \begin{bmatrix} \cos \alpha & -\sin \alpha \\ \sin \alpha & \cos \alpha \end{bmatrix} \dot{\mathbf{q}}_w \quad (3)$$

where  $\alpha$  is the orientation of the ASOC module with respect to the  $X$  axis in the inertial frame.

The kinematic relationship between the inertial velocity of the offset link joint  $C$  and the two wheel velocities is simply:

$$\dot{\mathbf{q}} = \mathbf{R} \mathbf{J}_w \mathbf{u} = \mathbf{J} \mathbf{u} \quad (4)$$

where  $\mathbf{J}$  is the Jacobian matrix for the ASOC module in the inertial coordinate frame  $XOY$ , which is given as:

$$\mathbf{J} = \begin{bmatrix} 1/2 \cos \alpha - S/D \sin \alpha & 1/2 \cos \alpha + S/D \sin \alpha \\ 1/2 \sin \alpha + S/D \cos \alpha & 1/2 \sin \alpha - S/D \cos \alpha \end{bmatrix} \quad (5)$$

The determinant of  $\mathbf{J}$  is:

$$\det \mathbf{J} = -S/D \quad (6)$$

This means that the ASOC module has no singularity, as long as the distance  $S$  is not zero.

By appropriately controlling the velocities of the two wheels of the ASOC module ( $V_1$  and  $V_2$ ), arbitrary and unique velocities at the joint  $C$  of the offset link can be achieved. Figure 3 shows the simulation results for an ASOC wheel module producing a velocity of 0.3 m/s in the  $X$  direction at the point  $C$ . The figure shows the starting configuration, the trajectory of the wheel module at the point  $O$ , and the velocities of the two wheels. The parameters for the simulation are  $D = 0.12$  m and  $S = 0.06$  m. It can be seen that the wheels follow a smooth trajectory while point  $C$  moves perpendicular to the connecting offset link. At first the two wheels move in opposite directions, but then converge to the same velocity. Although the wheels themselves cannot move perpendicular to their original orientations, the joint of the offset link can move in any direction instantaneously from any configuration. This is the fundamental feature of the ASOC design that enables it to achieve omni-directional mobility.

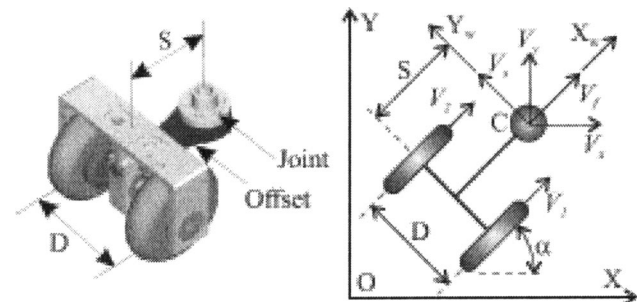


Fig. 2 An active split offset castor with its coordinate system

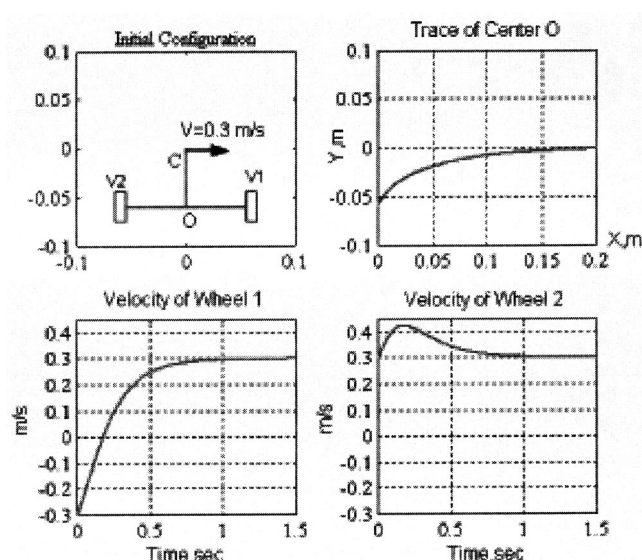


Fig. 3 Simulation of an ASOC unit performing sideward motion

### 3 Omni-Directional Platforms With ASOC Modules

If a platform or a vehicle is considered as a rigid body moving on a plane, its motion has three degrees of freedom ( $x$ ,  $y$ , and  $\phi$ ). These can be fully defined by the linear velocities at any two distinct points (see Fig. 4). If the velocities at these two points can be controlled arbitrarily subject to the constraint that the distance between these points remains fixed, omni-directional mobility for the platform can be achieved.

As shown in Section 2, the ASOC module can produce an arbitrary velocity at the joint of the offset link (point  $C$ ) by appropriate independent control of its two wheels. With a minimum of two ASOC modules, an omni-directional mobility platform can be constructed as illustrated in Fig. 4.

In the inertial coordinate frame, the velocities of the platform center,  $V_{cx}$ ,  $V_{cy}$ ,  $\Omega$ , and the velocities  $V_{x1}$ ,  $V_{y1}$ ,  $V_{x2}$ ,  $V_{y2}$  of the two ASOC modules at their joints,  $C_1$  and  $C_2$ , are defined as the follows:

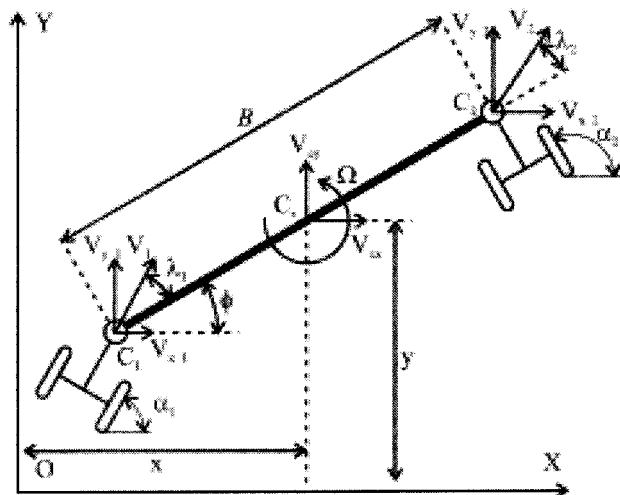


Fig. 4 A platform with ASOC modules

$$\begin{aligned}\dot{\mathbf{p}}_v &= [V_{cx} \ V_{cy} \ \Omega]^T \\ \dot{\mathbf{q}}_v &= [V_{x1} \ V_{y1} \ V_{x2} \ V_{y2}]^T\end{aligned}\quad (7)$$

where  $\Omega$  is  $d\phi/dt$ . The velocities of the platform can be expressed in terms of the velocities at the offset link joints as:

$$\dot{\mathbf{p}}_v = \mathbf{J}_v \dot{\mathbf{q}}_v \quad (8)$$

where:

$$\mathbf{J}_v = \begin{bmatrix} 1/2 & 0 & 1/2 & 0 \\ 0 & 1/2 & 0 & 1/2 \\ 1/B \sin \phi & -1/B \cos \phi & -1/B \sin \phi & 1/B \cos \phi \end{bmatrix} \quad (9)$$

Given the desired platform velocities, the joint velocities are obtained using the relative velocity kinematic relations between  $C_v$ ,  $C_1$ , and  $C_2$ . They are given as:

$$\dot{\mathbf{q}}_v = \mathbf{N}_v \dot{\mathbf{p}}_v \quad (10)$$

where  $\mathbf{N}_v$  is the  $4 \times 3$  matrix:

$$\mathbf{N}_v = \begin{bmatrix} 1 & 0 & B/2 \sin \phi \\ 0 & 1 & -B/2 \cos \phi \\ 1 & 0 & -B/2 \sin \phi \\ 0 & 1 & B/2 \cos \phi \end{bmatrix} \quad (11)$$

It should be noted that  $\mathbf{N}_v$  is not the inverse matrix of  $\mathbf{J}_v$  as  $\mathbf{J}_v$  is square and therefore not invertible. Rather,  $\mathbf{N}_v$  is derived from the kinematic relations and constraints of the system. The system has four inputs and three outputs, creating an over-constrained system. Once the joint velocities are determined using Eq. (11), the wheel velocities for the two wheels of each ASOC module can be determined using Eq. (4).

Vehicles with the ASOC design need at least two ASOC modules with a total of four actuators for three degrees of freedom. The physical constraint of the constant distance between the two offset link joints  $C_1$  and  $C_2$  is used to eliminate this apparent redundancy and leads to the following velocity constraint:

$$V_1 \cos \lambda_1 = V_2 \cos \lambda_2 \quad (12)$$

where  $V_1$  and  $V_2$  are the joint velocities of  $C_1$  and  $C_2$ , and  $\lambda_1$  and  $\lambda_2$  are the angles between the line connecting  $C_1$  and  $C_2$  and the respective joint velocity vectors (see Fig. 4).

Violating this constraint will result in wheel slippage and degrade the tracking performance of the system. The platform control algorithm must consider this constraint when calculating the desired wheel velocities. However, errors such as wheel and structure deformation under loads, floor irregularities, and wheel velocity control errors due to limited bandwidth and actuator saturation can make this calculation imprecise.

For the platform to move with velocities  $V_{cx}$ ,  $V_{cy}$ , and  $\Omega$ , the joint velocities,  $V_{x1}$ ,  $V_{y1}$ ,  $V_{x2}$ , and  $V_{y2}$ , are obtained from the inverse kinematics based on the orientation,  $\phi$ . Wheel velocities for each ASOC module are then resolved based on its orientation,  $\alpha$ . That means accurate knowledge of both  $\alpha$  and  $\phi$  is necessary for generating velocity commands that will not violate the constraint. In theory, the values of  $\alpha$  for each module and the orientation,  $\phi$ , could be obtained via a dead reckoning calculation using the wheel encoder signal. However, this is not a reliable calculation because any error due to wheel slippage can grow rapidly. Instead  $\phi$  is measured directly with localization sensors. For example, the SmartWalker has a vision based localization system that keys on external markers [9]. With knowledge of  $\phi$ , the platform velocities can be transformed into the body-fixed frame, and then the joint velocities can be computed in that frame. This eliminates the dependence on  $\phi$ . Optical encoders placed on each joint of the offset link are used to measure the angles  $\theta_1$  and  $\theta_2$  be-

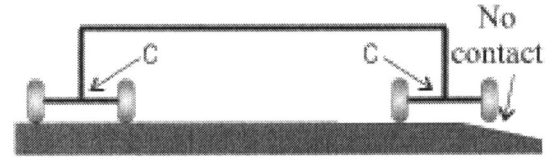


Fig. 5 Ground contact of ASOC modules on flat and uneven floor

tween the vehicle chassis and ASOC modules. For each ASOC module, the following relation is observed between  $\theta$ ,  $\alpha$ , and  $\phi$ :

$$\alpha = \theta + \phi \quad (13)$$

In the body-fixed platform,  $\phi$  is zero and  $\alpha$  is equal to  $\theta$ . Correct velocity commands can then be generated to satisfy the constraint given by Eq. (12) solely based on  $\theta$ . Therefore with the joint encoders, errors are contained with each sampling time and do not accumulate, which greatly improves the accuracy of the system.

#### 4 Operation on Uneven Floors

The simplest configuration of an omni-directional vehicle using this approach will have two ASOC modules and one conventional passive castor wheel for static support. For the vehicle to sustain control, all four driving wheels must maintain good traction and thus must remain in contact with the floor at all times. The basic design would require the floor to be perfectly flat to maintain contact. However, in practice floor irregularities such as wires, gaps, bumps at the joints between tile and carpet are unavoidable (see Fig. 5).

Although some compliance in the wheel and the mechanical structure will alleviate this problem to some degree, it is often not sufficient. To accommodate the floor unevenness a simple and effective solution is to add a passive rotary joint to each ASOC module at point  $C$ , which allows the wheel pair shaft,  $\overline{AC}$ , to rotate freely about the  $u$ -axis (see Fig. 6).

Below it is shown that by adding these passive joints all the wheels will maintain contact with an uneven floor. This is done by first showing that if two wheels of one ASOC touch the ground, the workspace of the second ASOC's wheels can lie on the ground. Then it is shown that any of the passive castors can touch the ground if they have proper independent suspensions.

Assume that the wheels are modeled as thin disks and  $P_1(x_1, y_1, z_1)$  is a point on the ground, then a second point,  $P_2(x_2, y_1, z_2)$ , is chosen to lie in the same plane,  $P_{xz}$ , as  $P_1$  with the constraint that:

$$d = \sqrt{(x_2 - x_1)^2 + (z_2 - z_1)^2} \quad (14)$$

where  $d$  is the distance between the two wheels (see Fig. 7).

If the ground is represented by  $z = f(x)$ , given  $x_1$ , it is possible to find  $z_1$ . Knowing  $x_1$  and  $z_1$  and using Eq. (14), the location of point  $P_2$  can be found. Assuming that the axle also lies in the  $XZ$  plane (which is reasonable for slightly uneven surfaces), the location of the point  $P_3(x_3, y_1, z_3)$ , which is the location of the joint in the ASOC, is determined.

Then by geometry, the point  $C$  is found by translating the point  $P_3$  along the  $Y$ -axis by a distance  $S$  (see Fig. 8). Using simple

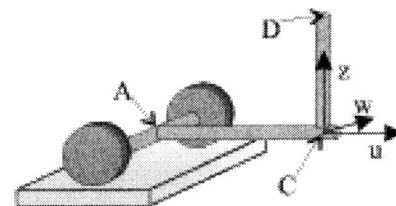


Fig. 6 Added passive joint to the ASOC



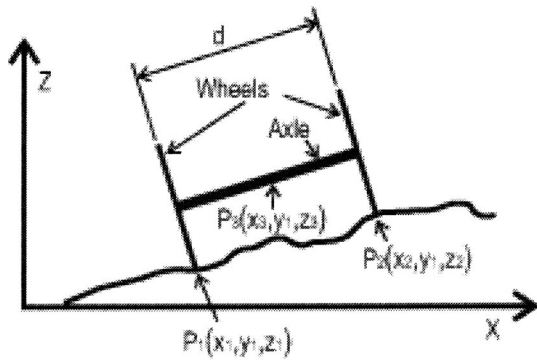


Fig. 7 ASOC on uneven terrain

kinematics, it can be shown that from point  $C$  the workspace of the point  $P'_3(x'_3, y'_3, z'_3)$ , the point on the second ASOC corresponding to  $P_3$ , is bounded by the inequality:

$$(h-s)^2 \leq (x'_3 - x_3)^2 + (y'_3 - (y_1 + s))^2 + (z'_3 - z_3)^2 \leq (h+s)^2 \quad (15)$$

where  $h$  is the length of the bar that attaches the ASOCs.

As long as the terrain exists inside of the workspace, which is true for all cases except when the terrain is a sphere with a radius less than  $(h+s)$ , then the point  $P'_3$  can exist at any height above the terrain. If that is the case, then the two points  $P'_1$  and  $P'_2$  can also exist. This is possible because given  $P_1$ , it is possible to find  $P_2$  and  $P_3$ . Conversely, given  $P'_3$  it is possible to find  $P'_1$  and  $P'_2$ . Thus, all four wheels of the two ASOCs can touch the ground at the same time on an uneven terrain. Designs without this rotary axis defined by the passive joint or some equivalent degree of freedom, will not operate properly on uneven floors.

The passive castors will contact the ground as long as they have a suspension that allows them to elongate linearly downward sufficiently to reach the ground. Thus, all of the wheels of an omni-directional platform based on the ASOC with the included suspension will touch the ground at all times.

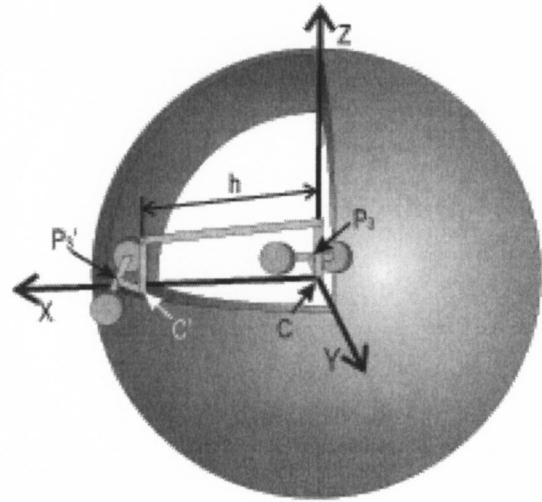


Fig. 8 Workspace of the second ASOC

It can also be shown that the dead reckoning accuracy of this omni-directional design is not significantly degraded by non-ideal (uneven) floors. This is done by performing a simulation where the wheel velocities are controlled by the equations derived in Section 2 for an ideal floor but the unevenness of the floor and the passive suspension joint are included in the simulation model. Obviously if the floor shape and angle of the passive suspension joint were known, any error due to floor unevenness could be compensated for by modifying the wheel velocities. However, it will be shown that for slightly uneven floors, the control algorithm derived for flat floors results in acceptable errors.

To model the system behavior given the wheel velocity inputs, the velocity of point  $D$  (see Fig. 6) must be determined. The angle of the passive suspension joint is  $\beta$ , its time derivative is  $\dot{\beta}$ , and  $\gamma_1$  and  $\gamma_2$  are the ground contact angles of the wheels (see Fig. 9).

Equation (16) represents the velocity of point  $D$ .

$$\begin{bmatrix} V_x \\ V_y \\ V_z \end{bmatrix} = \begin{bmatrix} \frac{1}{2}(V_1 \cos \gamma_1 + V_2 \cos \gamma_2) \cos \alpha + \sin \alpha \left( \frac{\dot{\beta} l (\cos^2 \beta - \sin^2 \beta)}{D} + \frac{1}{2}(V_1 \sin \gamma_1 + V_2 \sin \gamma_2) \sin \beta - \frac{S}{D} \cos \beta (V_1 - V_2) \right) \\ \frac{1}{2}(V_1 \cos \gamma_1 + V_2 \cos \gamma_2) \sin \alpha - \cos \alpha \left( \frac{\dot{\beta} l (\cos^2 \beta - \sin^2 \beta)}{D} + \frac{1}{2}(V_1 \sin \gamma_1 + V_2 \sin \gamma_2) \sin \beta - \frac{S}{D} \cos \beta (V_1 - V_2) \right) \\ \frac{1}{2}(V_1 \sin \gamma_1 + V_2 \sin \gamma_2) \cos \beta + \sin \beta \left( \frac{S}{D} (V_1 - V_2) - 2 \dot{\beta} l \cos \beta \right) \end{bmatrix} \quad (16)$$

Note that when  $\beta$ ,  $\dot{\beta}$ ,  $\gamma_1$ , and  $\gamma_2$  reduce to zero, the above equation reduces to Eq. 4.

Now using the equations derived in section 2 to control the

wheel velocities and applying them to the model given by Eq. (16) to determine the position of the omni-directional platform, the effect of floor unevenness and the passive suspension on the dead

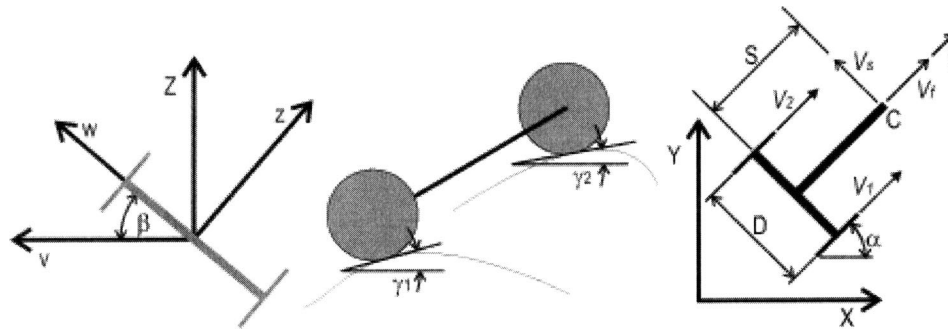


Fig. 9 Dimensions for the analysis on uneven floors

reckoning accuracy of the system can be evaluated. Consider the case where a bump on the floor is modeled by the function:

$$z = (amp)e^{-(peak*x)^2 - (peak*y)^2} \quad (17)$$

where  $amp$  gives the height of the bump in meters and  $peak$  regulates the sharpness of the bump. The simulation uses the dimensions of the SmartWalker, namely  $S = 35.8$  mm,  $D = 95$  mm, and  $l = 180$  mm. The deviation of point  $D$  from the desired path was found for bump heights ranging from 0 to 40 mm with a peak value of 15. The results show that point  $D$  only deviates from its intended path by approximately the height of the bump. Bumps on most indoor floors used by the SmartWalker would be in the range of 0 to 3 mm with a possible maximum height of 10 mm.

A simulation of the full omni-directional platform traversing uneven terrain is also done. In the case discussed below the distance between the two ASOCs is 0.5 m and the terrain is defined by the function:

$$z = amp \left( x^3 - \frac{(1-x)^2}{3} - \frac{x}{5} + y^5 \right) e^{-x^2 - y^2} \quad (18)$$

The results show that after traveling over 14 m, the omni-directional mobility platform returns to within 4 mm of its starting position (see Fig. 10). This is difficult to resolve from the figure, but it also indicates that a simple flat floor control algorithm would often be acceptable for use on uneven floors.

It should be noted that a number of other factors such as wheel compression under load and structural misalignment will also affect a platform's dead-reckoning accuracy. Often the system will

be provided with a closed loop local navigation system to correct for accumulated tracking errors. The SmartWalker uses a vision system that identifies and tracks local landmarks. However, a more accurate platform will place less computational demands on its closed loop control system.

## 5 Wheel Scrubbing Analysis

Wheel scrubbing in an omni-directional design using conventional wheels can be an important factor in both motor saturation and power consumption. For many omni-directional platforms limits on power requirements are important practical considerations. The SmartWalker uses batteries and increasing system efficiency increases the time between recharges.

Conventional wheels in general motion on a plane experience three main resistance forces: the contact friction,  $f$ , the rolling resistance,  $M_r$ , and the scrubbing torque,  $M_s$ . The scrubbing torque is the torque required to twist a single wheel around its vertical axis. Scrubbing torque can be very important in omni-directional platforms which use a single wheel twisted about a vertical axis [6]. The scrubbing torque can be calculated by integrating the frictional force elements over the entire contact patch between the wheel and the floor. To do this, the contact pressure distribution is calculated by treating the contact between a solid rubber wheel and a rigid floor as a Hertzian contact problem [10] where the normal pressure is multiplied by a coefficient of friction to yield the local shear stress [11]. Integrating the torque due to the shear stress over the contact area yields the scrubbing torque. For a cylindrical wheel (see Fig. 11(a)), the scrubbing torque is

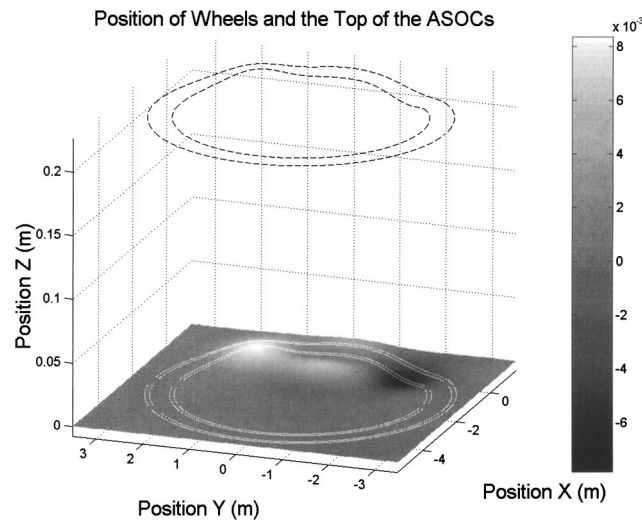


Fig. 10 Position of wheels and point  $D$  of the omni-directional mobility platform traversing uneven terrain

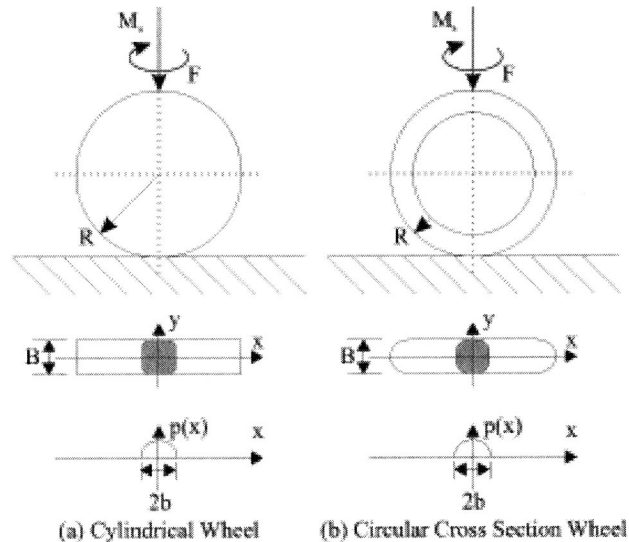


Fig. 11 Wheel contact patch and pressure distribution

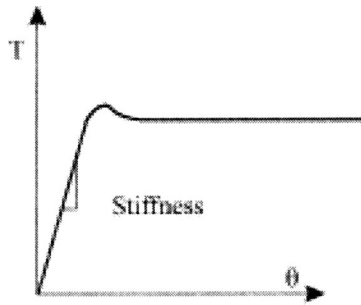


Fig. 12 Twisting torque as a function of twist angle

$$M_s = 4\mu \int_0^{B/2} \int_0^b \sqrt{x^2 + y^2} p(x) dx dy \quad (19)$$

where  $\mu$  is the coefficient of friction and  $p(x)$  is the Hertzian pressure distribution of the contact patch. For a wheel with a circular cross section (see Fig. 11(b)), the integration is:

$$M_s = \mu \int_0^b 2\pi x^2 p(x) dx dy \quad (20)$$

Equations (19) and (20) can be evaluated numerically.

For a single non-rolling wheel twisted around its vertical axis under the twisting moment  $T$ , there is no initial relative motion between the wheel material and the floor. Instead, the material deforms in the tangential direction. As  $T$  increases, this deformation reaches a limit, slippage (or scrubbing) occurs, and  $T$  reaches  $M_s$ . The relation between the twisting moment and the angle is represented in Fig. 12. The slope of the curve reflects the twisting stiffness of the wheel. This curve can be obtained with experimental methods [12]. It should be noted during the twisting of a single wheel, it is always the same part of the wheel material in the contact area that is rubbing against the floor. Each element of material in the contact area undergoes tangential deformation and experiences slippage.

In the case of a dual wheel pair separated by a distance,  $D$ , and under the same total load, each of the two wheels has a contact area similar in shape to the single wheel case, but the contact pressure is lower (see Fig. 13). When the wheel pair is twisted around its center for a full turn, the contact patches of the two wheels also undergo a full rotation, even though the pair does not have any forward motion.

In this case, when the wheel pair is twisted around its center at an angular velocity  $\omega_s$ , both of its wheels are rolling at a speed of  $V_0 = (D \cdot \omega_s)/2$ . The wheel material elements are impinging on the

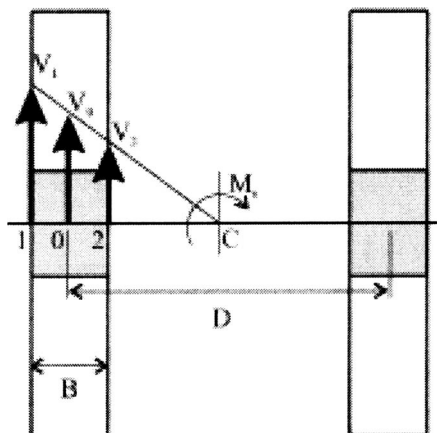


Fig. 13 Dual wheel set scrubbing analysis

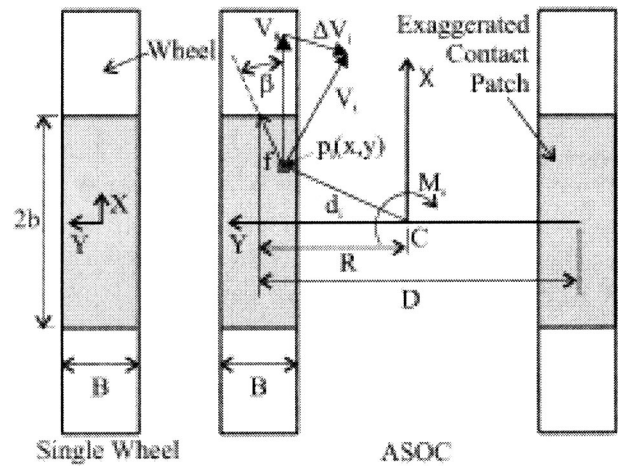


Fig. 14 Scrubbing torque of an element in the contact patch

floor at the speed  $V_0$ . The actual velocities at various points in the contact area are different. At any given instant some material touching the floor is being stretched and some is being compressed. Hence, deformation happens as the material elements make contact with the floor.

The tangential deformation of an element  $p_i(x,y)$  (see Fig. 14) within the contact patch can be expressed as the ratio of the velocity difference over the average rolling velocity,  $V_0$ , of the wheel, which is given as:

$$\varepsilon_i = \frac{\|\Delta \mathbf{V}_i\|}{\|V_0\|} = \frac{\|d_i - R\|}{R} \quad (21)$$

where  $d_i$  is the distance from the center of rotation,  $C$ , to the element in consideration. If  $\varepsilon_i$  does not reach a "breakaway strain" limit,  $\varepsilon_0$ , no scrubbing occurs in that element. However, if  $\varepsilon_i$  does reach the limit, the scrubbing torque of that element is given as:

$$\Delta M_s = \mu p(x,y) (x \sin \beta - y \cos \beta) dx dy \quad (22)$$

By integrating the contributing elements over the contact patch, the total scrubbing torque is obtained. In the single wheel case,  $\varepsilon_i$  at every point in the contact patch will eventually reach a limit  $\varepsilon_0$ , and slippage will occur, so every material element contributes the scrubbing torque. In the dual wheel case, however, at those points where  $\varepsilon_i$  is small, no slippage will occur before the elements move out of contact. Obviously if  $D$  is very large, both wheels will be essentially rolling on straight lines with virtually no scrubbing. Those material elements have no contribution to the scrubbing torque. Therefore, the total scrubbing torque for a wheel pair rotating around a fixed spot can be smaller than when a single wheel is twisted around the spot. However, wheel scrubbing can exist in the dual wheel design. The limit,  $\varepsilon_0$ , is a function of the wheel material and is determined experimentally. From Eq. (21), it also can be seen that  $\varepsilon_i$  does not depend on  $\omega_s$ , it depends on  $D$  only. Therefore, the total scrubbing torque depends on both wheel material and the wheel separation.

Figure 15 shows the calculated result of the total scrubbing torque of a dual wheel set as a function of the wheel separation distance. It shows that for elastic material, as expected the wheel scrubbing decreases as  $D$  increases. Moreover, as the elasticity of the wheel material increases, the wheel distance will have a bigger effect.

The above results show that the scrubbing torque of the dual wheel pair twisting about its central vertical axis depends on the wheel separation distance. A wheel in general planar motion has two velocities, rolling velocity  $V$  and turning velocity  $\omega$ . With the assumption that the wheel is not experiencing slip due to its forward rolling, the motion of the wheel can always be treated as if



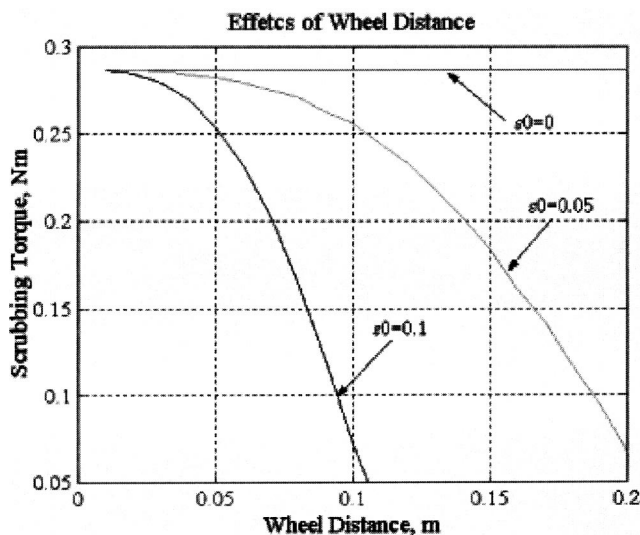


Fig. 15 Scrubbing torque versus wheel distance

it is being twisted around a point along the line perpendicular to its rolling velocity (see Fig. 13). This point is called the instantaneous center of rotation (ICR). The distance from the ICR to its vertical axis is  $D = V/\omega$ . Therefore, at any time, a single wheel in general motion can be treated as one of the two wheels in a dual wheel set with a wheel distance of  $D$ , and the scrubbing torque can be calculated. When the wheel is twisted without moving forward, the scrubbing torque is higher than when the wheel is moving at the same time. With this extension, the scrubbing torque, power and energy consumption can be calculated. Peak power and energy consumption are two key issues for self-contained systems, such as a robotic walker for the elderly or robotic transport vehicles in factories.

For an example, compare the scrubbing power of the ASOC design with the active castor wheel design when they perform the same motion. Consider the case where the castor is commanded to drive the chassis in a straight line to the right (see Fig. 16). The results show that the active castor has a higher scrubbing torque and higher total power consumption than the ASOC (see Fig. 17).

## 6 Application and Experimental Results

The ASOC design has been implemented as the mobility drive for an intelligent walker for elderly people, dubbed the SmartWalker [9,13,14]. The SmartWalker mobility system has two ASOC modules and two passive castors for static stability. Each wheel of the ASOC unit is driven by a DC motor with an optical encoder. Each offset link joint has an optical encoder for the mea-

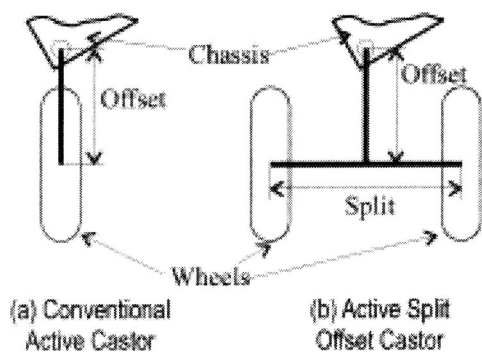


Fig. 16 Comparison between active castor and ASOC (top view)

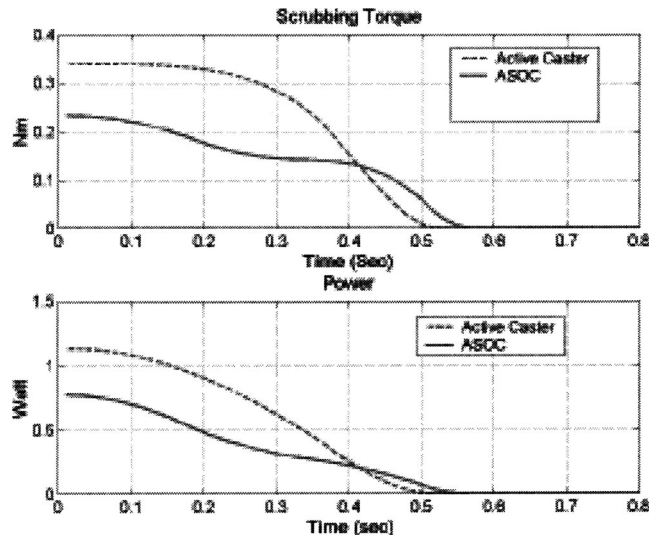


Fig. 17 Scrubbing torque and power dissipation for an active castor and an active split offset castor

surement of the joint angle. Figure 1 shows the detail of the ASOC module design used for the SmartWalker [13].

To evaluate the omni-directional mobility capabilities, a series of experiments was performed. For example, the SmartWalker was commanded to traverse a circular path and a square path. The SmartWalker was also tested on various floor conditions, such as carpet, concrete, and tile. Furthermore, the SmartWalker was commanded to run over bumps at doorframes and small pieces of debris. The SmartWalker demonstrated smooth motions in all these tests.

One of the most distinctive features of the mobility system is that it can simultaneously perform translational and rotational motions. Figure 18 demonstrates the SmartWalker moving forward in a straight line in the  $Y$  direction while rotating around its center counterclockwise. During the experiments, the actual position and orientation of the system are measured using the SmartWalker's vision based localization system [9]. The localization system continually measures the position and orientation of the platform in the inertial coordinate frame. The trajectory shown in the figure is the position of the camera, which is mounted at a distance of 0.18 m from the center. The omni-directional mobility is clearly dem-

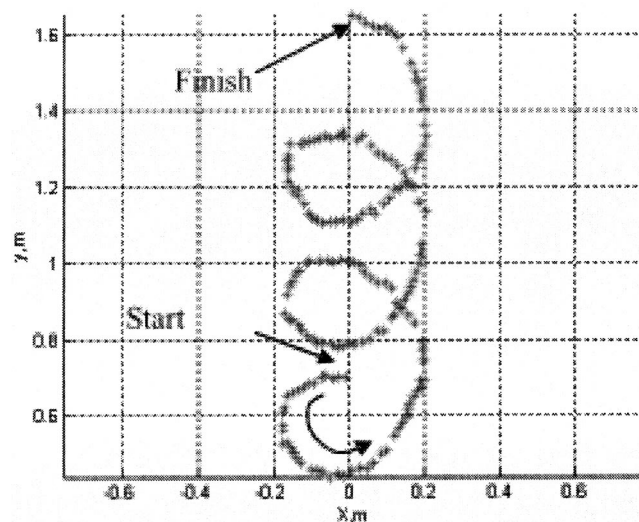


Fig. 18 Plot of a complex path executed by the SmartWalker

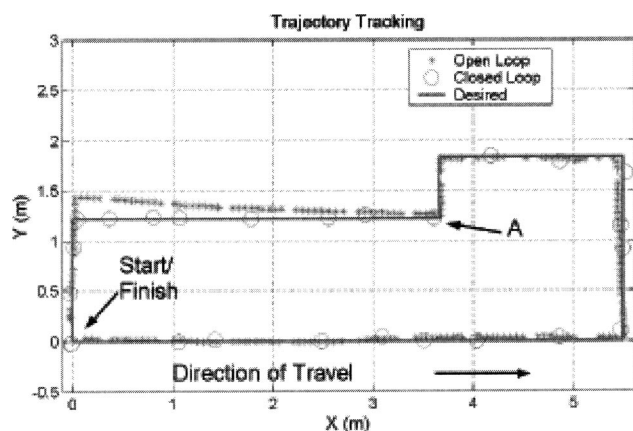


Fig. 19 Open vs. closed loop trajectory tracking

onstrated by the good cycloid trajectory of the camera. The small deviations from the perfect cycloid path are mainly due to the vision localization errors.

Further experiments were conducted to assess the trajectory tracking performance of the system. The walker is commanded to follow a trajectory that is about 15 meters long with several sharp turns (see Fig. 19). It travels at a constant speed of 50 cm/s. The maximum deviation from the path is less than 30 cm, which occurred when the walker makes a sharp turn over a part of the floor that changed from concrete to a waffle iron plate (point A in Fig. 19). Under closed loop control using the vision system for localization, the trajectory error is reduced to less than 10 cm.

## 7 Conclusions

In this paper, a concept for omni-directional mobility platform design based on the active split offset castor is presented. Each ASOC module has two coaxial and independently driven wheels and is connected to the platform via an offset link. An omni-directional platform can be constructed with a minimum of two ASOC modules and one passive castor. The advantages of the design over existing omni-directional platforms based on special wheel include a simple mechanical structure, high loading capacity, vibration free and smooth motion, and robustness to non-ideal floor conditions. This design has significantly lower wheel scrubbing compared with conventional active castor designs and is thus

more power efficient. The concept has been used as the mobility design for an intelligent walker for the elderly that has been demonstrated under clinical conditions [14]. The experimental results of the prototype demonstrated the system's omni-directional mobility with good tracking accuracy.

## Acknowledgments

This work was sponsored by the Home Automation and Healthcare Consortium in the MIT d'Arbelloff Laboratory for Information for Information.

## References

- [1] West, M., and Asada, H., 1997, "Design of Ball Wheel Mechanisms for Omnidirectional Vehicles with Full Mobility and Invariant Kinematics," *ASME J. Mech. Des.*, **119**(2), pp. 153–161.
- [2] Fujisawa, S., Ohkubo, K., Yoshida, T., Satonaka, N., Shidama, Y., and Yamaura, H., 1997, "Improved Moving Properties of an Omnidirectional Vehicle Using Stepping Motor," *Proc. of the 36th Conference on Decision & Control*, pp. 3654–3657.
- [3] Ferriere, L., and Rautent, B., 1998, "ROLLMOBS, a New Universal Wheel Concept," *Proc. of the IEEE International Conference on Robotics and Automation*, **3**, pp. 1877–1882.
- [4] Muir, P., and Neuman, C. P., 1987, "Kinematic Modeling for Feedback Control of an Omnidirectional Wheeled Mobile Robot," *Proc. of IEEE International Conference on Robotics and Automation*, **4**, pp. 1772–1778.
- [5] Killough, S. M., and Pin, F. G., 1994, "A New Family of Omnidirectional and Holonomic Wheeled Platforms for Mobile Robots," *IEEE Trans. Rob. Autom.*, **10**(4), pp. 480–489.
- [6] Borenstein, J., Everett, H. R., and Feng, L., 1996, *Navigating Mobile Robots*, AK Peters, Wellesley, Massachusetts.
- [7] Wada, M., and Mori, S., 1996, "Holonomic and Omnidirectional Vehicle with Conventional Tires," *Proc. of the IEEE International Conference on Robotics and Automation*, **4**, pp. 3671–3676.
- [8] Holmberg, R., and Khatib O., 1999, "Development of a Holonomic Mobile Robot for Mobile Manipulation Tasks," *Proc. of the Conference on Field and Service Robotics*, pp. 268–273.
- [9] Dubowsky, S., Genot, F., Godding, S., Kozono, H., Skwersky, A., Yu, L., and Yu, H., 2000, "PAMM—A Robotic Aid to the Elderly for Mobility Assistance and Monitoring: A Helping-Hand for the Elderly," *Proc. of the IEEE International Conference on Robotics and Automation*, **1**, pp. 570–576.
- [10] Hertz, H. 1895, *Gesammelte Werke*, **1**, Leipzig.
- [11] Slocum, A., 1992, *Precision Machine Design*, Prentice Hall, Englewood Cliffs, New Jersey.
- [12] Moore, D. F., 1975, *The Friction of Pneumatic Tires*, Elsevier Scientific Publishing Company, New York.
- [13] Spenko, Matthew, 2001, "Design and Analysis of the SmartWalker, a Mobility Aid for the Elderly" Master Thesis, Massachusetts Institute of Technology, Cambridge, MA.
- [14] Yu, H., 2002, "Mobility Design and Control of Personal Mobility Aids for the Elderly," Ph.D Thesis, Massachusetts Institute of Technology, Cambridge, MA.